High-order harmonic spectroscopy of the Cooper minimum in argon: Experimental and theoretical study

J. Higuet,[1] H. Ruf,[1] N. Thiré,[2] R. Cireasa,[2] E. Constant,[1] E. Cormier,[1] D. Descamps,[1] E. Mével,[1] S. Petit,[1] B. Pons,[1] Y. Mairesse,[1] and B. Fabre[1]

[1]*CELIA, UMR5107 (Université Bordeaux 1 - CNRS - CEA) 351, cours de la libération - F-33405 Talence Cedex France*

[2]*Laboratoire Collisions Agrégats Réactivité, (IRSAMC), UPS, Université de Toulouse and CNRS, UMR 5589, F-31062 Toulouse, France*

(Received 30 November 2010; published 2 May 2011)

We study the Cooper minimum in high-order-harmonic generation from argon atoms by using long wavelength laser pulses. We find that the minimum in high-order-harmonic spectra is systematically shifted with respect to total photoionization cross section measurements. We use a semiclassical theoretical approach based on classical trajectory Monte Carlo and quantum electron scattering methods to model the experiment. Our study reveals that the shift between photoionization and high-order-harmonic emission is due to several effects: the directivity of the recombining electrons and emitted polarization, and the shape of the recolliding electron wave packet.

DOI: 10.1103/PhysRevA.83.053401 PACS number(s): 42.65.Ky, 42.65.Re, 32.80.Rm

I. INTRODUCTION

High-order-harmonic generation (HHG) takes place when an atom or a molecule is submitted to a strong laser field (with intensities I in the range 10^{13}–10^{14} W/cm^2). Under the influence of the strong field, an electron can be tunnel-ionized, accelerated, and driven back to its parent ion where radiative recombination results in the emission of extreme ultraviolet (XUV) radiation [1,2]. While this process was initially considered as a secondary source of radiation, it was soon realized that it is closely related to photoionization and that it could thus encode structural information on the irradiated target. The first experimental observation that confirmed this link consisted of the appearance of a local minimum in the high-order-harmonic emission from argon atoms [3], which was associated to the Cooper minimum observed in XUV photoionization of argon [4]. In photoionization, it is well known that this minimum is due to a zero dipole moment between the p ground-state wave function and the d wave function of the photoionized electron for a photon energy of about 48 eV. Such minima have been extensively studied in photoionization because they constitute clearly identifiable features against which theoretical models can be tested.

The interest in structural minima in HHG was revived when the case of high-order harmonics from aligned molecules was considered, showing that minima encoding the molecular structure could appear in harmonic spectra [5]. Many works have since focused on observing these minima [6–13]. These studies have raised a number of questions on the modeling of the HHG process such as the influence of the ionic potential on the recolliding electron [14,15], the contribution of multiple molecular orbitals [10,16,17], the influence of the strong laser field [18,19], and the role of propagation effects [20]. Since some of these questions are still debated, and since HHG from molecules is quite complex to model, we decided to come back to the simpler case of high-order harmonics from atoms.

In this paper, we study the Cooper minimum in high-order-harmonic emission from argon atoms using tunable infrared (1800–2000 nm) femtosecond laser pulses. We perform a systematic experimental study of the position of the minimum as a function of the laser field (intensity and wavelength) and macroscopic parameters (gas pressure, beam focusing conditions). We find a systematic shift of more that 5 eV in the position of the minimum with respect to total photoionization cross section measurements [21,22]. We perform a theoretical study to understand the origin of this shift and find that it is partly due to the difference between angle-integrated photoionization measurements with unpolarized light and the HHG recombination process, which is highly differential with respect to both electron and polarization directions. Using a semiclassical simulation based on a combination of classical trajectory Monte Carlo (CTMC) [23] and quantum electron scattering techniques (QUEST), we show that the additional contribution to the shift is due to the shape of the recolliding electron wave packet. This new theoretical description, which we refer to as CTMC-QUEST, properly accounts for the influence of the ionic potential on the recolliding electron wave packet and is thus able to reproduce accurately the experimental high-order-harmonic spectra.

This paper is organized as follows. In Sec. II, we describe the experimental setup and present measurements of the Cooper minimum under various laser and macroscopic conditions. In Sec. III, we analyze the analogies and differences between photoionization and recombination using quantum electron scattering theory. Finally, we perform in Sec. IV a complete simulation of the experiment combining CTMC and QUEST approaches. Atomic units are used throughout the paper unless otherwise stated.

II. EXPERIMENT

A. Experimental setup

It is well known [24] that harmonic spectra generally consist of a rapid decrease of yield for low harmonic orders, followed by a plateau which extends up to the cutoff photon energy at $\sim 3.17U_p + 1.3I_p$, where U_p is the laser ponderomotive energy $U_p = I/(4\omega_0^2)$, with ω_0 the laser frequency, and I_p is the target ionization potential ($I_p = 15.76$ eV for Ar) [25]. Therefore, an accurate determination of the position of the Cooper minimum in HHG can be achieved provided the minimum belongs to the plateau region of the spectrum. Since the minimum lies around 50 eV, this requires laser intensities above 2×10^{14} W/cm^2; close to the saturation intensity of

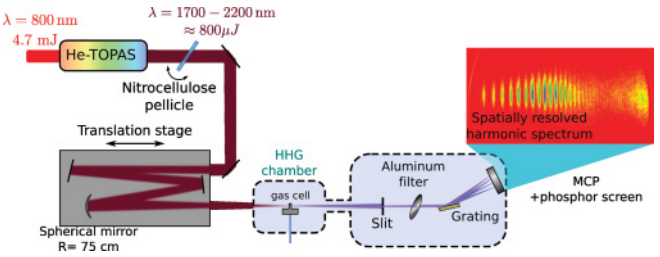

FIG. 1. (Color online) Experimental setup (see text).

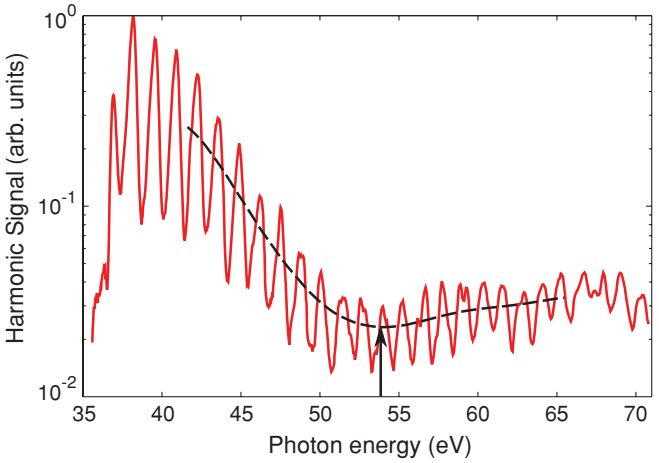

FIG. 2. (Color online) High-order-harmonic spectrum generated in argon by a 1830 nm, 8×10^{13} W/cm^2, 50 fs laser pulse. The spectrum is averaged over 25 000 laser shots. The dashed line is a Gaussian smoothing of the spectrum. The arrow indicates the position of the Cooper minimum at $E = 53.8$ eV.

argon when using 800 nm, ∼40 fs laser pulses. A way to perform measurements at higher intensities is to use few-cycle laser pulses: Wörner *et al.* recently measured the Cooper minimum in Argon at I up to 3.5×10^{14} W/cm^2 using 8 fs 780 nm laser pulses [26]. We have chosen an alternative solution to obtain a high cutoff; namely, by using a long wavelength driving laser [27–29]. The cutoff frequency scales as $I \times \lambda^2$, making it possible to produce 100 eV photons at less than 1×10^{14} W/cm^2 using 1800 nm fs pulses.

The experimental setup is presented in Fig. 1. We use the 1-kHz Aurore laser system from CELIA which delivers 800 nm, 7 mJ, 35 fs pulses. We reduce the pulse energy to 4.7 mJ and inject it to a HE-TOPAS parametric amplifier (Light Conversion Ltd.). We use the idler from the TOPAS to get 800 μJ pulses, continuously tunable between 1700 and 2200 nm. These pulses are focused by a 75-cm-radius spherical silver mirror into a 2 mm continuous gas cell filled with argon (backing pressure around 50 mbar). The pulse energy can be adjusted by rotating a 30-μm-thick nitrocellulose pellicle, whose transmission varies from ∼95% under normal incidence to ∼50% under ∼70° incident angle. The high-order harmonics are sent to an XUV flat field spectrometer consisting of a 250 μm slit, a 1200 mm^{-1} (variable groove spacing) grating (Hitachi), a set of dual microchannel plates (MCPs) associated with a phosphor screen (Hamamatsu), and a 12-bit cooled CCD camera (PCO).

An important item in the experimental setup is a 200-nm-thick aluminum filter placed before the spectrometer. Indeed, high-order-harmonic radiation produced by the 1800 nm pulses can extend to more than 100 eV. Our study deals with measurements of the Cooper minimum, around 50 eV. Since the high-order-harmonic emission from argon is quite efficient around 100 eV, while it is a minimum around 50 eV [28], the second-order diffraction of the 100 eV radiation by the grating can significantly affect the shape of the spectrum at 50 eV. We have observed this effect as a bump which fills in the Cooper minimum as the laser energy increases. The aluminum foil in our experiment filters out the radiation above 73 eV, ridding us of this artifact.

The proper calibration of our XUV spectrometer is crucial to accurately determine the position of the Cooper minimum. The incidence angle of the grating is accurately set by using a precision rotation mount. The distances between the source and the grating and between the grating and MCP are measured. The central wavelength of the fundamental radiation is measured using a near infrared spectrometer. From all these parameters we can determine the theoretical position of the different harmonics on the MCP, assuming a certain order q_0 for the first harmonic. We compare these theoretical positions to the measured positions and determine the value of q_0 that provides good agreement. Since we measure many harmonics, we can check the fine agreement of the calculated and measured positions over a broad spectral range. We can finely adjust the distance between the grating and MCP, which is subject to the biggest uncertainty in our experiment, to achieve perfect agreement and extract the pixel-wavelength conversion function. As a check of the calibration, we measure the transmission of the aluminum foil in our experimentand compare it to the theoretical transmission of a 200-nm-thick filter with a 5 nm layer of alumina on each side [30]. The position of the abrupt cutoff in the filter transmission is in excellent agreement.

A typical harmonic spectrum obtained at a laser wavelength of 1830 nm is shown in Fig. 2. The spectrum was normalized to take into account the pixel-wavelength conversion, the diffraction efficiency of the grating, and the measured transmission of the aluminum filter. An additional advantage of using long wavelengths appears in this spectrum; that is, the fundamental photon energy is 0.68 eV so that the spectrum is more dense than at 800 nm (to which corresponds a photon energy of 1.55 eV), making the determination of the position of the minimum more accurate. The dashed line in Fig. 2 is a Gaussian smoothing of the spectrum, from which we extract the location of the Cooper minimum. We performed a series of identical measurements to evaluate the average position of the minimum and obtained $E = 53.8 \pm 0.7$ eV.

B. Systematic study

In order to check the robustness of the position of the Cooper minimum against experimental conditions, we have performed a systematic study of HHG in argon, varying both the laser field parameters, which control the single-atom response, and the macroscopic parameters (gas pressure, beam focusing conditions), which influence the HHG yield that is ultimately detected.

1. Laser field parameters

An important difference between HHG and photoionization experiments is the presence of a strong laser field, which might modify the position of the Cooper minimum. We thus conducted a study as a function of the laser field parameters (intensity and wavelength).

Figure 3(a) shows a few harmonic spectra produced at different laser intensities (controlled by rotating the nitrocellulose pellicle). As the intensity increases, the cutoff is shifted from 60 to 90 eV. The laser intensity is estimated by means of the well-known $1.3I_p + 3.17U_p$ behavior of the cutoff of the measured HHG spectra [25]. The Cooper minimum is clearly visible in all spectra. Figure 3(b) shows the measured position of the minimum as a function of the laser intensity. We do not observe any systematic variation of the minimum location as the intensity is increased twofold, even if the ponderomotive energy changes by more than 10 eV. The positions at lower intensities are slightly below average but, because the signal is smaller, the error bars are larger. We also varied the central wavelength of the laser pulses delivered by the HE-TOPAS between 1800 and 1980 nm [Fig. 3(c)]. We do not observe any significant shift in the Cooper minimum, which stays around 53.8 eV. These two observations constitute strong indications of the lack of influence of the laser field on the recombination process.

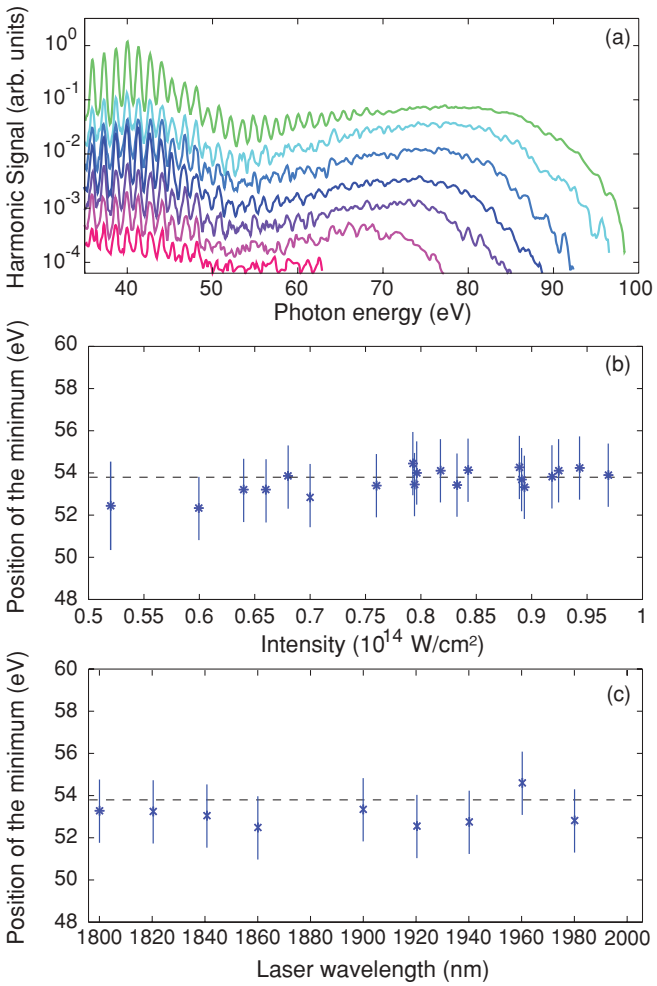

FIG. 3. (Color online) (a) High-order-harmonic spectra generated in argon by a 1830 nm, 50 fs laser pulse at intensities between 5×10^{13} W/cm^2 (bottom) and 8×10^{13} W/cm^2 (top). No aluminum filter was used for these spectra. The spectra are arbitrarily shifted vertically with respect to each other. Each spectrum is averaged over 25 000 laser shots. (b) Position of the Cooper minimum in argon as a function of laser intensity at 1830 nm and (c) as a function of laser wavelength. The horizontal dashed line marks the previously determined minimum-location value; $E = 53.8$ eV.

2. Phase matching

While the Cooper minimum is a characteristic of high-order-harmonic emission from a single atom, our experiment measures the outcome of a macroscopic process. It is thus important to evaluate the possible influence of propagation effects in the measured spectra [31]. To do that, we varied several parameters which affect the phase matching conditions and the macroscopic buildup of the harmonic signal. First, we varied the backing pressure of the gas cell between 12 and 160 mbar and did not observe any change in the position of the Cooper minimum [Fig. 4(a)]. Second, we varied the

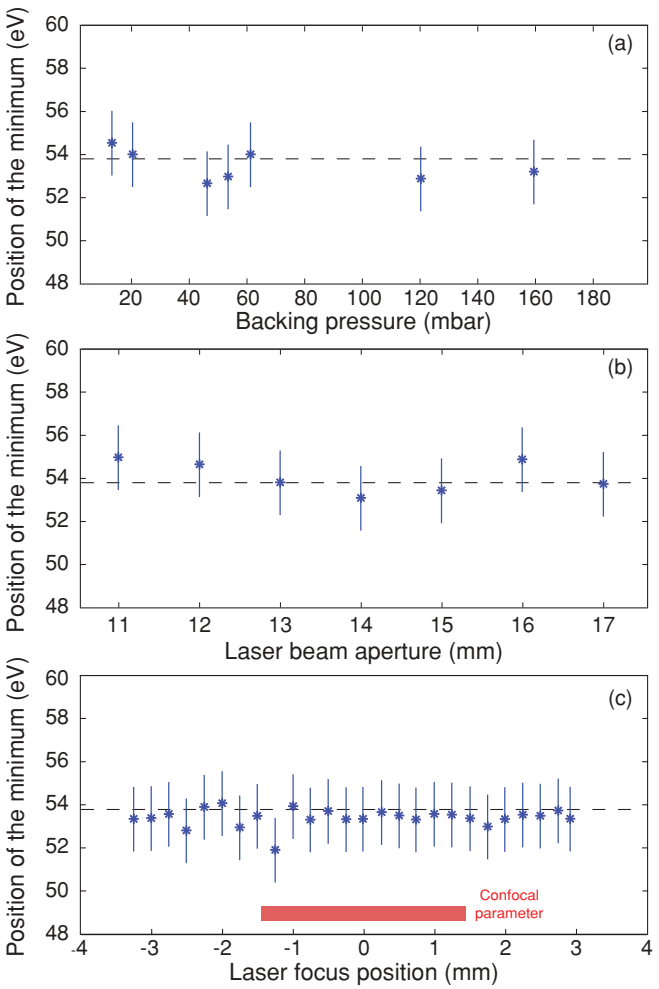

FIG. 4. (Color online) Position of Cooper minimum in argon at 1830 nm as a function of backing pressure in mbar (a), laser beam aperture (b), and longitudinal position of the focus (c). The horizontal dashed line marks the previously determined minimum-location; $E = 53.8$ eV.

laser beam aperture between 11 and 17 mm. This resulted in a modification of the harmonic cutoff but did not change the position of the Cooper minimum [Fig. 4(b)]. Finally, we varied the longitudinal position of the laser focus with respect to the center of the gas cell [Fig. 4(c)]. This also led to a change of the cutoff position but the location of the minimum remained the same. We note that we did not observe any signature of the presence of long trajectories in our experiment while scanning the focus position. The harmonics always appear spatially collimated and spectrally narrow, which indicates that the short trajectories are always favored in our generating conditions.

These observations are different from what has recently been reported by Farrell *et al.* in a study of the Cooper minimum in argon using 800 nm pulses [32].

III. PHOTOIONIZATION AND RADIATIVE RECOMBINATION

Our experimental study has shown that the Cooper minimum in HHG is located at 53.8 eV. This position is different from that measured in photoionization spectra (between 48 and 49 eV). Although at first sight photoionization and recombination appear to be strictly reverse processes, which would lead to a simple conjugation relation between the associated transition dipoles, the experimental observations show a systematic shift. In this section, we perform a detailed theoretical analysis of the link between photoionization and radiative recombination processes in order to explain this difference.

Our calculations rely on the single active electron (SAE) approximation [33], where the description of electron dynamics is restricted to that of a single Ar valence electron. The interaction of this electron with the nucleus and other electrons is reproduced, in the framework of a mean-field theory, by the model potential [34]

$$V(r) = -\frac{1}{r} - \frac{A\,e^{-Br} + (17 - A)\,e^{-Cr}}{r}, \tag{1}$$

with $A = 5.4$, $B = 1$, and $C = 3.682$. This model potential fulfills the correct asymptotic condition [i.e., $V(r \to \infty) = -1/r$] and the expected behavior at the origin [$V(r \to 0) = -18/r$]. In [34], the parameters A, B, and C were adjusted so as to provide the correct I_p(Ar); we have further checked that $V(r)$ yields accurate values for the energies of the Ar(nl) excited states with $n \geqslant 4$.

The diagonalization of the hydrogen-like Hamiltonian $\mathcal{H} = p^2/2 + V$ in a basis of even-tempered Slater-type orbitals (STO) yields bound and discretized continuum states in the spherical form $\Psi_{n,l,m}(\mathbf{r}) = R_{n,l}(r)Y_l^m(\Omega)$ where Y_l^m are spherical harmonics of a given (l,m) symmetry and $\Omega_\mathbf{r} \equiv (\theta_\mathbf{r},\varphi_\mathbf{r})$ is the angular $\hat{\mathbf{r}}$ direction. The scattering continuum states $\Psi_\mathbf{k}$, normalized on the wave-vector scale $\mathbf{k}$, are developed in the spherical state basis

$$\Psi_\mathbf{k}(\mathbf{r}) = \frac{1}{k}\sum_{l=0}^{\infty}\sum_{m=-l}^{l} (\imath)^l e^{\imath\delta_{k,l}}\; R_{k,l}(r)(-1)^m Y_l^m(\Omega_\mathbf{r})Y_l^{-m}(\Omega_\mathbf{k}), \tag{2}$$

where $\Omega_\mathbf{k} \equiv (\theta_\mathbf{k},\varphi_\mathbf{k})$ corresponds to the angular $\hat{\mathbf{k}}$ direction. Since the diagonalization of $\mathcal{H}$ in the STO underlying basis yields a coarse-grained representation of the continuum [35,36], we alternatively obtain the radial parts $R_{k,l}(r)$ and the phase shifts $\delta_{k,l}$ (including both Coulombic and short-range components) through direct integration of the radial Schrödinger equation, using the Numerov algorithm. It is important to note that Eq. (2) explicitly includes the influence of the ionic core on the ejected and recombining electron, beyond the plane-wave approximation which does not allow a faithful description of either photoionization or HHG [26,37].

A. Photoionization cross section

The photoionization rate induced by absorption of a radiation of amplitude F_0 and polarization axis $\mathbf{n}$ is given by the Fermi's golden rule [33]:

$$w(\mathbf{k},\mathbf{n}) = \frac{\pi}{2}k|\langle\Psi_\mathbf{k}|\,\mathcal{D}\,|\Psi_{3,1,0}\rangle|^2, \tag{3}$$

where $\mathcal{D} = -F_0\mathbf{n}\cdot\mathbf{r}$ is the electric dipole moment operator. The photoionization differential cross section is given by

$$\frac{d^2\sigma}{d\Omega_\mathbf{k}d\Omega_\mathbf{n}} = \frac{4\pi^2}{c}k\omega|\langle\Psi_\mathbf{k}|\,\mathbf{n}\cdot\mathbf{r}\,|\Psi_{3,1,0}\rangle|^2, \tag{4}$$

where ω is the frequency of the ionizing photon and is related to the electronic momentum by the relation $\omega = I_p + k^2/2$.

We aim to compare our calculations to photoionization measurements of Marr and West [21] and Samson *et al.* [22]. In these experiments, the measured quantity is the total photoionization cross section, which includes all possible relative orientations between the electronic momentum and light-polarization axis:

$$\sigma(k) = \int\int \frac{d^2\sigma}{d\Omega_\mathbf{k}d\Omega_\mathbf{n}}d\Omega_\mathbf{k}d\Omega_\mathbf{n}. \tag{5}$$

Because of the selection rules for electric dipole transitions, the calculation of $\langle\Psi_\mathbf{k}|\,\mathbf{n}\cdot\mathbf{r}\,|\Psi_{3,1,0}\rangle$ is reduced to the components of $\Psi_\mathbf{k}$ whose angular momenta are $l = 0$ ($p \to s$ transition) and $l = 2$ ($p \to d$ transition). The angular part of this calculation can be done analytically, and the total photoionization cross section can finally be expressed as

$$\sigma(k) = \frac{16\pi^3\omega}{9kc}\left(I_{k,0}^2 + 2I_{k,2}^2\right), \tag{6}$$

where c is the speed of light and $I_{k,l}$ are the radial integrals $I_{k,l} = \int R_{k,l}(r)R_{3,1}(r)r^3dr$. These radial integrals are plotted in Fig. 5. $I_{k,0}$ is positive whatever the value of k and slowly decreases as the electron energy increases. The $p \to d$ integral exhibits stronger modulations and a sign change for an electron kinetic energy of 30.6 eV (corresponding to a photon energy of 46.3 eV). This sign change is responsible for the minimum observed in the calculated total photoionization cross section, as seen in Fig. 6.

Our calculation shows a clear minimum in the photoionization cross section for a photon energy of 50.1 eV, slightly above the measured value (between 48 an 49 eV). The agreement with the experiment is fairly good, except for low photon energies (below 30 eV), as usual in single active electron calculations. In order to perform accurate calculations in this energy range, one has indeed to take into account multielectronic effects and transitions to excited states of the neutral [38].

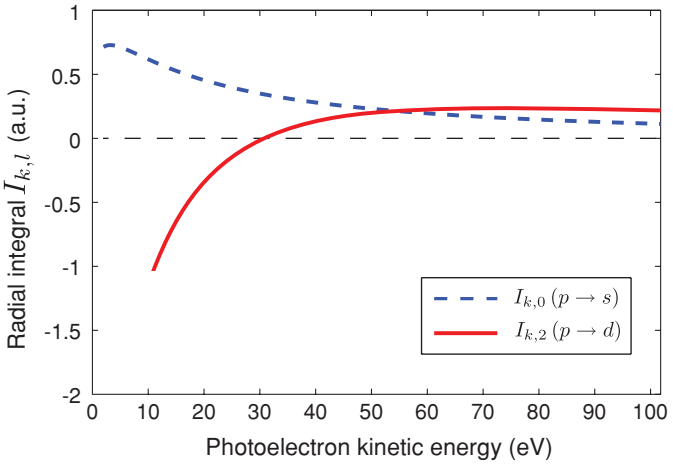

FIG. 5. (Color online) Radial integrals $I_{k,l}$ associated with $p \rightarrow s$ (dashed line) and $p \rightarrow d$ (plain line) transitions.

B. Recombination dipole in HHG

1. Linear laser field

An important specificity of high-order-harmonic generation compared to photoionization is the selection of specific values of **k** and **n**. First, tunnel ionization selects the quantization axis of the atomic orbital (z) parallel to the polarization axis of the ir generating field, as recently confirmed experimentally [39–41]. The ir field drives the trajectory of the recombining electron along the same axis. The electronic momentum **k** thus has to be taken parallel to the quantization axis of the orbital. Furthermore, from symmetry considerations, the emitted XUV field has to be parallel to the common axis of the laser polarization and quantization. The calculation is thus reduced to the case of $\hat{\mathbf{k}} \parallel \mathbf{n} \parallel \hat{\mathbf{z}}$.

Within this framework, the recombination matrix element is equal to

$$|d_{\mathrm{rec}}|^2 = |\langle \Psi_{\mathbf{k}} | \mathbf{n} \cdot \mathbf{r} | \Psi_{3,1,0} \rangle|^2 = \frac{1}{12\pi k^2} |I_{k,0} e^{\imath \delta_{k,0}} - 2 I_{k,2} e^{\imath \delta_{k,2}}|^2. \quad (7)$$

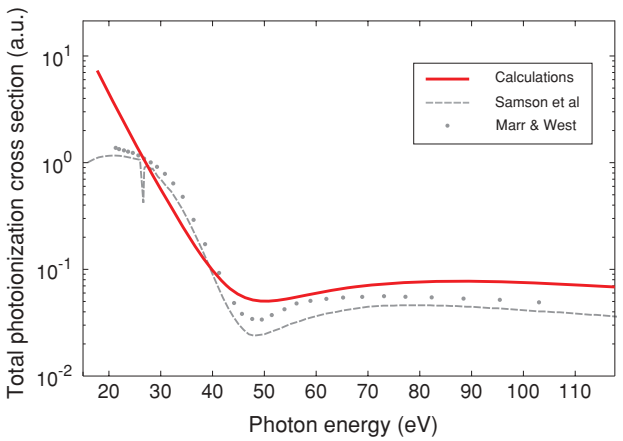

FIG. 6. (Color online) Calculation of the total photoionization cross section (plain line) compared to measurements from [21] (dotted line) and [22] (dashed line).

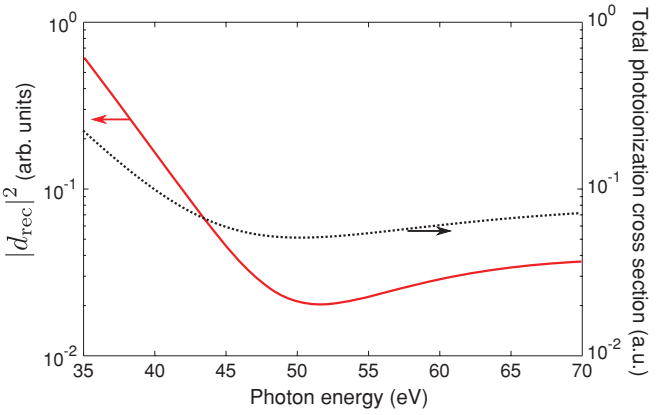

FIG. 7. (Color online) Calculation of $|d_{\mathrm{rec}}|^2$ (plain line) compared to total photoionization cross section (dashed line).

The evolution of $|d_{\mathrm{rec}}|^2$ as a function of the emitted photon energy is plotted in Fig. 7. The dipole moment shows a Cooper minimum which is more contrasted than that observed in the total photoionization cross section. This is due to the coherent nature of the differential cross section. The differential calculation leads to a coherent sum of the $p \rightarrow s$ and $p \rightarrow d$ transitions, which depends on the values of the scattering phases $\delta_{k,0}$ and $\delta_{k,2}$. In the case of angular integrated calculations, this phase influence vanishes, leading to an incoherent sum of the two contributions.

The Cooper minimum in the recombination dipole moment is located at 51.6 eV, while it is at 50.1 eV in the total photoionization cross section. The selection of the quantization axis and light polarization thus leads to a significant shift of the Cooper minimum. In the following, we confirm the importance of this selection by considering the case of an elliptical laser field.

2. Elliptical laser field

The recollision direction of the electron in HHG can be manipulated using an elliptically polarized laser field. In that case, the electron trajectory between tunnel ionization and recombination is two dimensional, the recollision axis is not parallel to the quantization axis and the polarization direction of the harmonics is not that of the laser field [42].

We have performed classical calculations to study the influence of ellipticity on the Cooper minimum in the framework of the so-called "Simpleman" model [1] that neglects the influence of the ionic potential on the electron dynamics between tunnel ionization and recombination. The electron trajectory is supposed to be ionized at time t_i through tunneling along the instantaneous field direction which sets the quantization axis; this accordingly yields the initial conditions $\mathbf{r}(t_i) = \mathbf{0}$ and $v_{\parallel}(t_i) = 0$. We further require the trajectory to be closed [i.e., $\mathbf{r}(t_r) = \mathbf{0}$ where t_r is the recombination time]. This imposes a nonzero perpendicular velocity at time of ionization, $v_{\perp}(t_i) \neq 0$, consistent with the lateral confinement of the electronic wave packet during tunneling. The recollision angle $\theta_{\mathbf{k}}$, which is defined with respect to the quantization axis and determines the $\hat{\mathbf{k}}$ direction at time of recombination [43], is then collected for each electron trajectory. This finally allows

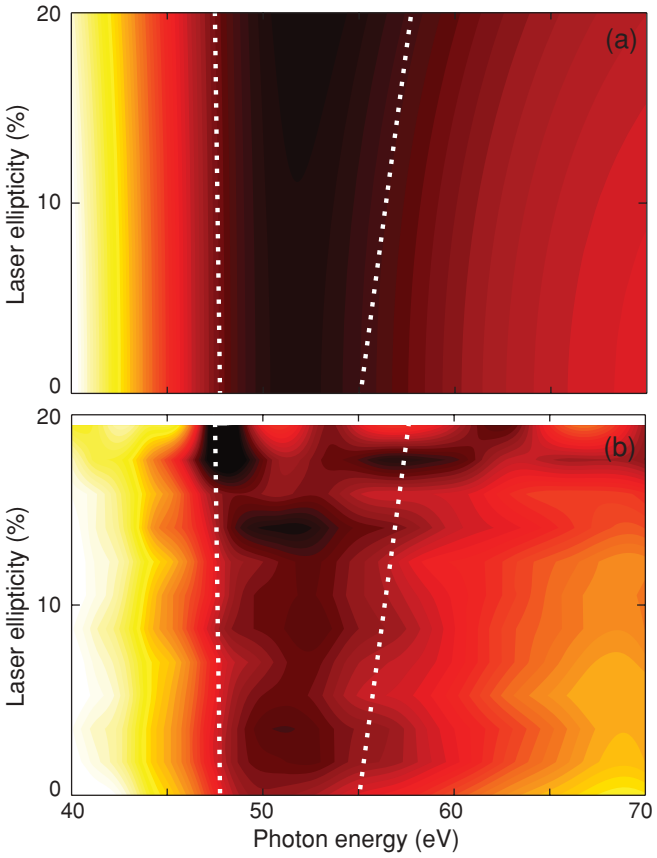

FIG. 8. (Color online) (a) Calculation of $|d_{\rm rec}(k,\theta_{\mathbf{k}})|^2$ as a function of photon energy and ellipticity of the driving field ($\lambda = 1900$ nm, $I = 1 \times 10^{14}$ W/cm^2). (b) Measured harmonic spectra in the same conditions. The dotted white lines are the same in the two panels.

us to compute the parallel $d_{\parallel}$ and orthogonal $d_{\perp}$ components of the recombination dipole.

In Fig. 8(a), we represent the value of $|d_{\rm rec}(k,\theta_{\mathbf{k}})|^2 = |d_{\parallel} + d_{\perp}|^2$ as a function of the generating field ellipticity ϵ for $\lambda = 1900$ nm and $I = 1 \times 10^{14}$ W/cm^2. As ϵ increases, the overall shape of the minimum is modified: it becomes broader on the high-energy side, with an approximate slope of 0.15 eV by percent of ellipticity. This behavior stems from increasing contributions of $\theta_{\mathbf{k}} \neq 0$ recombination angles to the HHG signal as ϵ increases, given that the minimum of $|d_{\rm rec}(k,\theta_{\mathbf{k}})|^2$ shifts to higher energy as $\theta_{\mathbf{k}}$ increases.

We performed measurements to confirm the broadening of the Cooper minimum by inserting a quarter waveplate in the laser beam. The ellipticity was controlled by rotating the axis of the waveplate with respect to the laser polarization. As ϵ increases the harmonic signal falls rapidly, preventing measurements with ellipticities larger than 20%. Figure 8(b) shows the normalized harmonic spectra as a function of the laser ellipticity, at an intensity of 1×10^{14} W/cm^2 and a laser wavelength $\lambda = 1900$ nm. The white dotted lines are identical in the two panels, which enables a direct comparison. As predicted by our simulations, the Cooper minimum broadens on the high-energy side as we increase ϵ with an average slope of approximately 0.2 eV by percent of ellipticity. These results confirm the important role of the recollision direction in the accurate determination of the shape of the harmonic spectrum even in a simple atomic system like Ar.

Although the calculated dipole moments and measured harmonic spectra show very similar shapes, there is still a systematic 2.2 eV shift between the positions of the measured and calculated Cooper minima. This is due to the fact that the harmonic spectrum $S(\omega)$ is determined not only by the recombination dipole moment $|d_{\rm rec}(k,\theta_{\mathbf{k}})|^2$ but also by the number of recombining electrons at each energy (i.e., by the shape of the recolliding electron wave packet). In the following, we use a CTMC approach to take this effect into account and compare it to the result of our experiment.

IV. COMPLETE THEORETICAL DESCRIPTION: CTMC-QUEST

In order to get a full description of the HHG process that includes the influence of the structure of the recolliding electron wave packet, we have developed a semiclassical theoretical simulation called the classical trajectory Monte Carlo quantum electron scattering theory (CTMC-QUEST). Our theory is based on a combination of classical and quantum approaches in the modeling of the HHG process. It is largely inspired by the well-known three-step model of laser-matter interactions [1], in which most of the processes subsequent to the primary field-induced ionization are determined by the recollision of the returning wave packet with the ionic core. In this respect, the strong field approximation (SFA) [25], which does not account for the ionic potential in the description of the motion of the freed electron, explicitly leads to an HHG yield represented as a product of the flux of returning electrons and the photorecombination cross section [6,44]. Such a factorized form of the HHG yield has also been analytically deduced from the time-dependent effective range (TDER) theory, in the limit of low-frequency excitation fields with $\omega \ll I_p$ [45]. Drawing from these studies, the HHG factorization has been generalized, assuming that the returning wave packet is insensitive to the features of the ionic potential. For instance, the high-energy end of the HHG responses of atoms has been simulated using electron propagation factors issued from short-range TDER calculations [46]. The case of complex targets has been considered in the framework of the so-called quantitative rescattering theory (QRS) [14], which is also based on the recollision picture [47]. In the QRS, the returning electron wave packet is obtained by means of the SFA or time-dependent Schrödinger calculations of an easily solvable model system with I_P similar to that of the target that is effectively considered.

Our semiclassical model also employs the factorization scheme for the calculation of the HHG yield. However, we aim at avoiding approximate computations of the electron wave packet. We therefore use CTMC simulations that treat the laser and ionic fields on a same footing to build the returning wave packet in terms of electron trajectories which fulfill preselected rescattering conditions. Once the wave packet is defined, quantum rescattering theory is used to compute the recombination probability and associated HHG spectrum.

A. CTMC and initial phase-space distribution

The CTMC method has originally been developed to describe nonadiabatic processes in atomic collisions [23]. It has been successfully applied to shed light on subtle ionization mechanisms [48,49] that cannot be represented unambiguously by purely quantum mechanical treatments. CTMC calculations have also been performed to describe laser-matter interactions (see e.g., [50–52]). As in atomic collisions, the classical assumption inherent in the CTMC method is not prohibitive in the description of field-induced processes; for instance, CTMC trajectories leading to HHG have been shown to match their quantum counterparts obtained in the framework of an hydrodynamical Bohmian description of the electron flow [53].

The CTMC approach employs an $\mathcal{N}$-point discrete representation of the phase-space distribution $\varrho(\mathbf{r},\mathbf{p},t)$ in terms of independent electron trajectories $\{\mathbf{r}_j(t),\mathbf{p}_j(t)\}$:

$$\varrho(\mathbf{r},\mathbf{p},t) = \frac{1}{\mathcal{N}} \sum_{j=1}^{\mathcal{N}} \delta(\mathbf{r}-\mathbf{r}_j(t))\delta(\mathbf{p}-\mathbf{p}_j(t)), \tag{8}$$

where $\mathbf{p}$ is the canonical momentum conjugate to $\mathbf{r}$. The temporal evolution of the ϱ distribution is governed by the Liouville equation, which is the classical analog to the time-dependent Schrödinger equation

$$\frac{\partial \varrho(\mathbf{r},\mathbf{p},t)}{\partial t} = -\frac{\partial \varrho(\mathbf{r},\mathbf{p},t)}{\partial \mathbf{r}}\frac{\partial H}{\partial \mathbf{p}} + \frac{\partial \varrho(\mathbf{r},\mathbf{p},t)}{\partial \mathbf{p}}\frac{\partial H}{\partial \mathbf{r}}, \tag{9}$$

where $H = \mathcal{H} + \mathbf{r}\cdot\mathbf{F}(t) = p^2/2 + V(r) + \mathbf{r}\cdot\mathbf{F}(t)$ is the total electronic Hamiltonian, including the laser-target interaction $\mathbf{r}\cdot\mathbf{F}(t)$ expressed in the length gauge. In our calculations, we use a simple sinusoidal laser field $F(t) = F_0\sin(\omega t)$ where $t \in [0,4\pi/\omega]$. This description reduces the interaction of a real shaped laser pulse with a macroscopic medium to a simplified scheme where the harmonic signal is generated by a single atom submitted to an effective laser field intensity. This simplification is justified by the insensitivity of the experimental results to macroscopic effects and to the laser intensity.

Inserting Eq. (8) into Eq. (9) yields the Hamilton equations which tailor the motion of the jth classical trajectory among the set of $\mathcal{N}$ independent trajectories:

$$\begin{aligned} \frac{\partial \mathbf{r}_j(t)}{\partial t} &= \mathbf{p}_j(t) \\ \frac{\partial \mathbf{p}_j(t)}{\partial t} &= -\nabla_{\mathbf{r}}[V(r)+\mathbf{r}\cdot\mathbf{F}(t)]|_{\mathbf{r}_j(t)}, \end{aligned} \tag{10}$$

The last equation emphasizes how the electron evolves under the combined action of the ionic and laser fields, beyond the widely used SFA that neglects. This has important consequences on the description of radiation and electron emission processes close to the ionization threshold [54,55].

The most common way to define an initial distribution is to use a microcanonical distribution whose energy is $-I_p$. In Fig. 9, we compare the quantum radial probability density $4\pi r^2 R_{3,1}^2(r)$ of the initial $3p$ Ar state to its microcanonical counterpart $\rho_M(-I_p;r,t=0) = \int\int \varrho_m(-I_p;\mathbf{r},\mathbf{p},t=0)d\mathbf{p}d\Omega_{\mathbf{r}} = 16\pi^2 r^2 \mathcal{C}\sqrt{2[-I_p+V(r)]}$ where $\mathcal{C}$ is a normalization constant. Besides the fact that

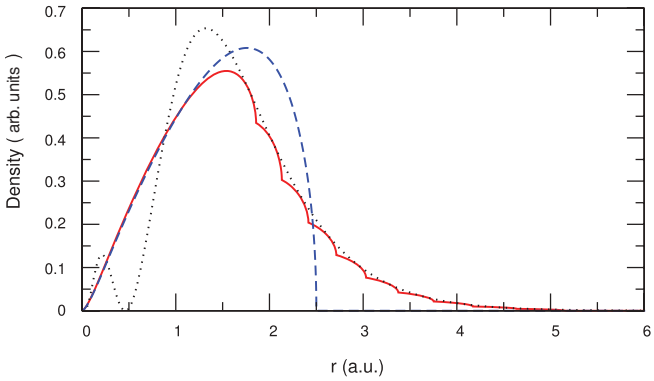

FIG. 9. (Color online) Comparison between the initial density $\rho(r,t=0)$ as a linear combination of ten microcanonical distributions (plain line), $\rho_M(-I_p;r,t=0)$ the one microcanonical distribution (dashed line), and the quantum radial electronic density of the fundamental Ar $3p$ state (dotted line).

$\rho_M(r,t=0)$ does not reproduce the nodal structure of the quantum $R_{3,1}^2(r)$, it restricts the electron density to an inner region close to the nucleus ($r \lesssim 2.5$) where ionization processes are classically less probable. Such a distribution can thus not properly describe the ionization.

Better quantitative results can be obtained in the framework of the CTMC approach, provided that one employs an improved initial distribution $\varrho(\mathbf{r},\mathbf{p},t=0)$, beyond the usual microcanonical description $\varrho_m(-I_p;\mathbf{r},\mathbf{p},t=0)$ which affects $-I_p$ to the energy of all $\mathcal{N}$ trajectories [56].

Improving the initial condition is based on the observation that a trajectory with energy $E_j(t=0) = p_j^2(t=0) + V(r_j(t=0)) \neq -I_p$ can participate in the description of the initial state since the negative part of the classical energy scale is not quantized. In other words, one can construct an improved initial phase-space distribution as a functional integral over microcanonical ones:

$$\varrho(\mathbf{r},\mathbf{p},t=0) = \int_{E^-}^{E^+} c(E)\varrho_M(E;\mathbf{r},\mathbf{p},t=0)\,dE, \tag{11}$$

where the bounds E^- and E^+ are given by the partition of the classical phase space into adjacent and nonoverlapping energy bins $[E^-,E^+[$ for a given l. The partition is made following the method explained in [57]; for Ar($3p$) this leads to $E^- = -1.885$ and $E^+ = -0.150$ for a classical momentum $|\mathbf{L}| = |\mathbf{r}\times\mathbf{p}|$ enclosed in $[1,2[$. In practice, the improved $\varrho(\mathbf{r},\mathbf{p},t=0)$ consists of a discrete representation of Eq. (11) in terms of ten microcanonical distributions. The (discretized) coefficients c_{E_m} are obtained by fitting the quantum radial probability density to $\rho(r,t=0) = \sum_{m=1}^{10} c_{E_m}\rho_M(E_m;r,t=0)$ with the additional condition that $\langle E_\rho\rangle = -I_p$.

The final $\rho(r,t=0)$ is displayed in Fig. 9. While the nodal structure of the quantum density still remains beyond the scope of the improved classical description (as expected), the newly defined $\rho(r,t=0)$ nicely matches the outer region of $R_{3,1}^2(r)$ from which classical electrons preferentially escape subject to the laser field. Finally, our improved calculations employ $\mathcal{N} = 20\times10^6$ trajectories in order to minimize statistical uncertainties.

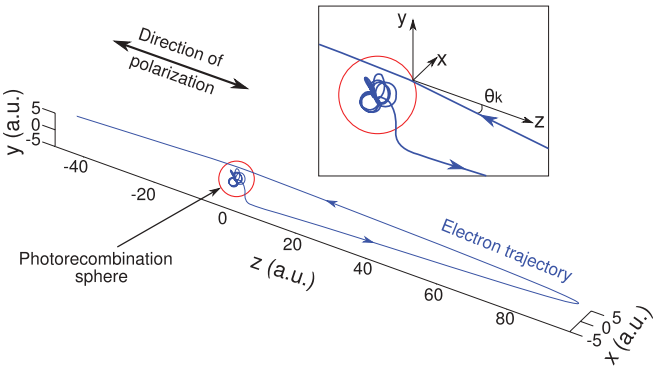

FIG. 10. (Color online) Typical short electron trajectory that contributes to the harmonic signal. The electron, after being ionized and leaving the sphere, comes back into it. The inset shows the recombination angle θ_k when the electron is recombining.

B. CTMC and returning electrons

We now address the definition of the rescattering electron wave packet. We define a rescattering sphere, centered on the target nucleus, of radius $R_{\rm rec}$ of the order of the extension of the fundamental wave function. Within the classical recollision picture, this sphere mimics the fundamental target state. We consider that an electron is rescattering and will generate a harmonic photon through recombination if, after being ionized and leaving the sphere, it comes back into it. Figure 10 shows a typical short electron trajectory which contributes to the harmonic signal. The recombination time is taken as the time at which the electron enters back into the sphere. We record the energy E_j and the direction $\hat{\mathbf{k}}$ of the wave vector at this instant. Within the CTMC statistics, we are thus finally able to define the density of the returning wave packet at time t:

$$\varrho_{\rm ret}(E,\hat{\mathbf{k}},t) = \frac{1}{\mathcal{N}} \sum_{i=1}^{\mathcal{N}_{\rm ret}(t)} \delta(E_i(t)-E)\delta(\hat{\mathbf{k}}_i(t)-\hat{\mathbf{k}}), \quad (12)$$

where $\mathcal{N}_{\rm ret}(t)$ is the number of electron trajectories that fulfill, at time t, the rescattering criterion mentioned above. Similarly, the phase $\Phi_{\rm ret}(E,\hat{\mathbf{k}},t)$ of the wave packet can be obtained according to

$$\Phi_{\rm ret}(E,\hat{\mathbf{k}},t) = \frac{1}{\mathcal{N}} \sum_{i=1}^{\mathcal{N}_{\rm ret}(t)} \phi_i(t)\delta(E_i(t)-E)\delta(\hat{\mathbf{k}}_i(t)-\hat{\mathbf{k}}), \quad (13)$$

where $\phi_i(t)$ is the phase accumulated along the ith electron path:

$$\phi_i(t) = \int_0^t [\mathbf{p}^2(t')/2 - V(r(t')) - \mathbf{r}(t')\cdot\mathbf{F}(t')]\,dt'. \quad (14)$$

Despite the seemingly random-like behavior of the trajectories before ionization (see Fig. 10), it has to be noted that the phases $\phi_i(t)$ of the $\mathcal{N}_{\rm ret}$ trajectories that contribute to HHG in (13) evolve identically as functions of time, since not only the release but also the recombination times of all these $\mathcal{N}_{\rm ret}$ trajectories are almost identical (see Fig. 11). Before ionization, $\Phi_{\rm ret}(E,\hat{\mathbf{k}},t) \sim I_P t$. In what follows, we shall not consider the phases because we are mostly interested in the shape and not the fine structure of the wave packet and associated HHG spectrum.

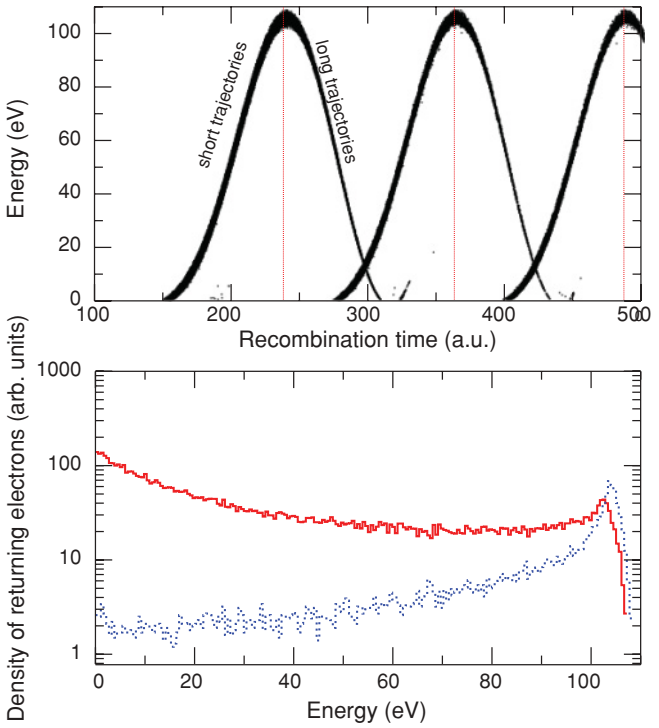

FIG. 11. (Color online) (a) Total energy of the returning electron as function of the photorecombination time. This representation permits a direct and intuitive separation of the different trajectories. In this figure, we only represent the long and short trajectories and omit the multiple returnings. (b) Representation of the density of returning electrons for short (—) and long (· · ·) trajectories.

Figure 11 shows typical features of the returning wave packet for $I = 10^{14}$ W/cm^2 and $\lambda = 1830$ nm. By monitoring the energy of the returning electron with respect to the recombination time [Fig. 11(a)] we can identify the short (plain line) and long (dotted line) trajectories. This is an important asset of CTMC-QUEST—the separation of the different classes of trajectories (short, long, or even multiple return ones) is natural.

In Fig. 11(b), we plot the time- and angle-integrated density of returning electrons for long and short trajectories:

$$\rho_{\rm ret}(E) = \int_0^\tau \int \varrho_{\rm ret}(E,\hat{\mathbf{k}},t)\,d\hat{\mathbf{k}}\,dt. \quad (15)$$

The density of returning electrons $\rho_{\rm ret}(E)$ increases with energy for long trajectories whereas it decreases for short trajectories. In other words, $\rho_{\rm ret}(E)$ decreases as the trajectory length increases. Two opposite effects are at play to determine the evolution of $\rho_{\rm ret}(E)$ with trajectory length. First, longer trajectories are born at earlier times when the laser field is more intense and thus benefit from a stronger ionization rate. However, longer trajectories also show a stronger lateral spread during propagation in the continuum, which reduces the number of recombining electrons. Our study shows that the latter effect is dominant. It is consistent with the fact that we do not observe long trajectories in our experimental study.

Within the classical recollision picture, the photorecombination sphere mimics the fundamental target state. The sphere radius is accordingly choosen to reproduce the extension of the

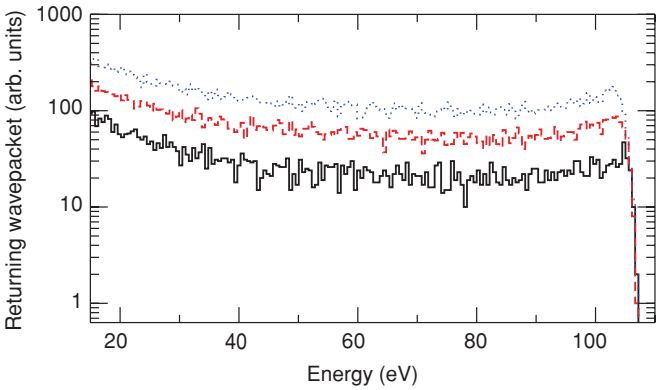

FIG. 12. (Color online) Comparison of the convergence for different radius size $R_{\rm rec} = 3$ (plain line), 5 (dashed line), and 7 a.u. (dotted line) of the photorecombination sphere for the short trajectories.

initial quantum state ($r_{\rm max} \sim 5$ a.u. in Fig. 9), independently from the excitation-laser conditions. Beyond such intuitive arguments, it is important to explicitly check that varying $R_{\rm rec}$ about the $r_{\rm max}$ value does not induce drastic changes in the shape of the returning wave packet; in other words, it is important to check that our calculations have converged. We accordingly present in Fig. 12 the $\rho_{\rm ret}(E)$ densities obtained for $R_{\rm rec} = 3$, 5, and 7 a.u. There is no significant difference between the shapes of the wave packets issued from the three calculations, which means that the convergence is good. In the following, we will thus use a photorecombination sphere of $R_{\rm rec} = 5$ a.u.

Our results can be compared to those obtained by Levesque *et al.* [44] who used experimental spectra and dipole moments calculated within the plane wave approximation (PWA) to extract the amplitude of the recolliding electron wave packet. The lower wavelength of the driving field (800 nm) employed by Levesque *et al.* cannot explain the sharp disagreement between their results and our results. While the shape of our wave packet falls by (only) a factor of ~5 in a 100 eV energy interval, several orders of magnitude appear between the low- and high-energy signals in [44]. We checked that this discrepancy is due to the use of PWA by dividing our experimental HHG spectrum of Fig. 2 by the square of the dipole moment computed in the PWA and recovering the drastic decrease of $\rho_{\rm ret}(E)$ as E increases. This confirms the importance of taking into account the influence of the ionic potential in all the three steps of the laser-matter interaction.

We can also compare our results to the quantitative rescattering theory (QRS) calculations from Le *et al.* (see Fig. 2 of [14]). In the QRS framework, the amplitude of the electron wave packet slightly depends on the method employed to compute the HHG spectrum. Le *et al.* display a flat-shaped wave-packet amplitude, as a function of E, when TDSE calculations are used to compute the spectrum, before dividing it by the dipole moment. Significant deviations are obtained at low E when the SFA is employed. We have performed (but do not show for sake of conciseness) similar calculations to those of Le *et al.* who employed an 800 nm driving pulse. This has allowed us to ascertain that, at 800 nm, the shape of $\rho_{\rm ret}(E)$ is indeed flat from low to high E when integrating over all trajectories and multiple returns, as is the case in TDSE calculations.

C. QUEST

The photorecombination probability $\mathcal{P}_{PR}(E,\hat{\mathbf{k}},t)$ is quantum mechanically obtained by using the microreversibility principle and Fermi's golden rule:

$$\mathcal{P}_{PR}(E,\hat{\mathbf{k}}) = \mathcal{P}_{PI}(\mathbf{k}') = \frac{\pi\sqrt{2E}}{2}|\langle\Psi_{E,\hat{\mathbf{k}}}|\,\mathbf{n}\cdot\mathbf{r}\,|\Psi_{3,1,0}\rangle|^2, \quad (16)$$

where $\Psi_{E,\hat{\mathbf{k}}}$ is the stationary scattering wave function for a total energy E and a wave-vector direction $\hat{\mathbf{k}}$. In the case of photoionization, the electron wave vector $\mathbf{k}'$ is related to the kinetic energy at infinity through $E = k'^2/2$. Recombination occurs at short range where the total electron energy reads $E = k^2/2 + V(R_{\rm rec})$. The analogy between photoionization and photorecombination is thus only respected if one sets $k' = \sqrt{2E}$.

In the first part of the paper, we calculated photorecombination probabilities by assuming that the electron trajectory was linear and parallel to the quantization axis. In the present statistical three-dimensional (3D) modeling, this is no longer the case. The electron escapes from $\mathbf{r} \neq \mathbf{0}$ with a nonzero transverse velocity; its interaction with the ionic potential can further deviate its trajectory from a straight line. Therefore, it is necessary to take the recombination angle θ_k into account, defined with respect to the z axis, in the computation of the photorecombination probability:

$$\mathcal{P}_{PR}(E,\hat{\mathbf{k}}) = \frac{\sqrt{2E}}{24}|I_{E,\hat{\mathbf{k}},0}e^{i\delta_{E,\hat{\mathbf{k}},0}} - I_{E,\hat{\mathbf{k}},2}(3\cos^2\theta_k - 1)e^{i\delta_{E,\hat{\mathbf{k}},2}}|^2. \quad (17)$$

D. CTMC-QUEST for HHG

Once the density of returning electrons and photorecombination probabilities are determined, we can calculate the harmonic spectrum $S(\omega,\hat{\mathbf{n}},t)$ as

$$S(\omega,\hat{\mathbf{n}},t) = \int dE\,\varrho_{\rm rec}(E,\hat{\mathbf{k}},t)\mathcal{P}_{PR}(E,\hat{\mathbf{k}})\delta(E + I_p - \omega) = \frac{1}{\mathcal{N}}\sum_{i=1}^{\mathcal{N}_{\rm ret}(t)}\mathcal{P}_{PR}(E_i(t),\hat{\mathbf{k}}_i(t))f(E_i(t),\omega), \quad (18)$$

where $f(E_i(t),\omega) = 1$ if $E_i(t) = \omega - I_p$ and 0 otherwise. In case of a laser field linearly polarized along the z axis $\hat{\mathbf{n}} = \hat{\mathbf{z}}$. The time-integrated HHG spectrum is simply obtained through $S(\omega,\hat{\mathbf{n}},\tau) = \int_0^\tau S(\omega,\hat{\mathbf{n}},t)dt$ where τ is the pulse duration.

1. *Role of returning electron wave packet*

In Fig. 13, we display the statistical distribution of the recombination probabilities $\mathcal{P}_{PR}(E_i(t),\hat{\mathbf{k}}_i(t))$ associated to all the short trajectories that lead to HHG during the whole interaction. This distribution consists of a set of scattered points in the $(E,\mathcal{P}_{PR}(E,\hat{\mathbf{k}}))$ plane (see inset in Fig. 13). The distribution is very narrow since $\theta_{k_i} \sim 0$ for most of the

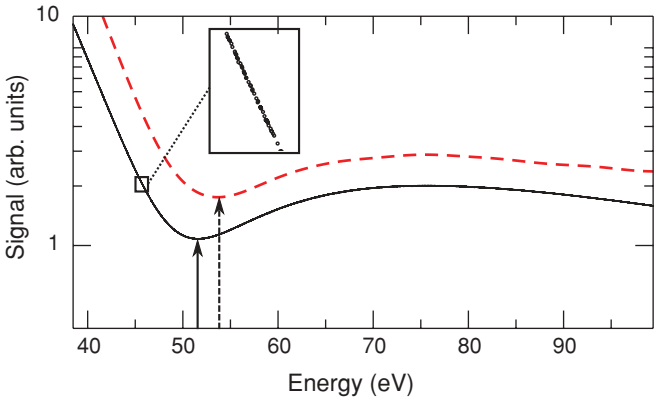

FIG. 13. (Color online) Comparison between the statistical distribution of recombination probabilities (scattered points which look like a plain line, see inset for details) and the harmonic spectrum (dashed line) for short trajectories obtained by CTMC-QUEST. The position of the Cooper minimum is shifted toward high energy for the harmonic spectrum. This is a consequence of the shape of the density of returning electrons.

trajectories so that its shape is similar to that of the dipole of Fig. 7.

The time-integrated HHG spectrum $S(\omega,\hat{\mathbf{n}},\tau)$ built according to Eq. (18) with only short trajectories is included in Fig. 13. This spectrum does not exhibit the typical peaks centered on the odd harmonics because we do not include the $e^{i\omega t}$ phase term in the definition of the HHG field [see Eq. (18)]; additional structures due to interferences between different electron paths cannot show up since $S(\omega,\hat{\mathbf{n}},\tau)$ is restricted to only the contribution of short trajectories. The position of the Cooper minimum in $S(\omega,\hat{\mathbf{n}},\tau)$, located at $E = 53.5 \pm 0.5$ eV, is different from the one obtained in the probability distribution. The latter one, found at $E = 51.7 \pm 0.5$ eV, is close to the value obtained assuming $\theta_{k_i} = 0$ for all the trajectories. The difference of minimum locations is mainly due to the shape of the recolliding electron wave packet for short trajectories [Fig. 11(b)]: the decrease of $\rho_{\mathrm{ret}}(E)$ with increasing E shifts the minimum observed in the photorecombination probability distribution to higher energies. This result, obtained on a simple atomic system, demonstrates that the accurate study of orbital structure via HHG cannot be restricted to the study of the dipole moment. The shape of the returning wave packet also has to be accurately known.

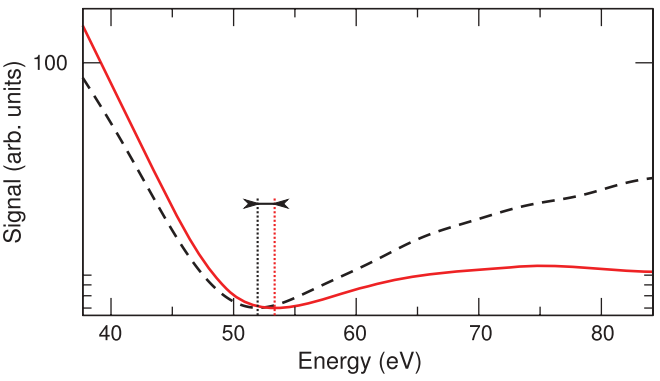

FIG. 14. (Color online) Comparison between the theoretical harmonic spectrum obtained either for long (dashed line) or short (plain line) trajectories. As expected from the shape of the returning wave packet, the position of the Cooper minimum is different for these two types of trajectories.

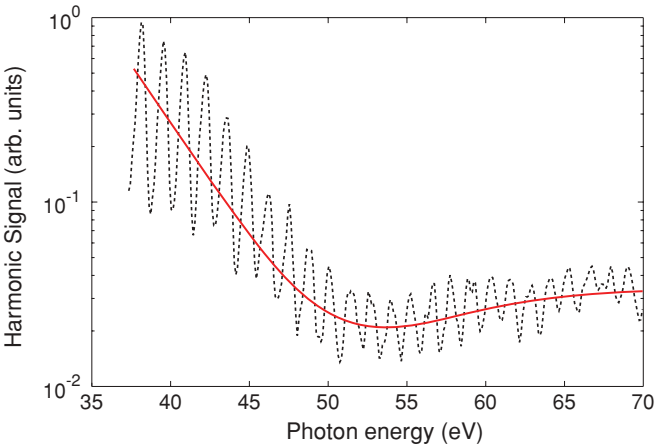

FIG. 15. (Color online) Comparison between experimental (dashed line) and CTMC-QUEST (full line) spectra obtained with a 1830 nm laser field at 1×10^{14} W/cm^2.

The importance of the shape of the recolliding wave packet is confirmed in Fig. 14 where we compare the harmonic spectra generated by the short and the long trajectories. Interestingly, the position of the Cooper minimum is sensitive to the considered set of trajectories; it stands at 51.7 eV for long trajectories and at 53.7 eV for short ones. This behavior is due to the opposite slopes of the electron wave-packet profiles [see Fig. 11(b)].

2. *Comparison with experiments*

Figure 15 shows a comparison between experimental and theoretical HHG spectra for $\lambda = 1830$ nm and $I = 10^{14}$ W/cm^2. The agreement is very satisfactory since the position of the theoretical Cooper minimum is 53.7 eV which nicely matches the experimental minimum of 53.8 ± 0.7 eV. The overall shape of the experimental spectrum is also very well described.

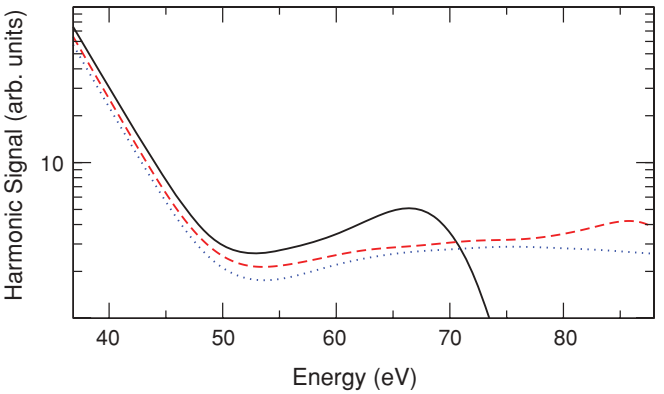

FIG. 16. (Color online) CTMC-QUEST spectra obtained with a 1830 nm laser field at 5×10^{13} (plain line), 7.5×10^{13} (dashed line), and 1×10^{14} W/cm^2 (dotted line).

In Fig. 16, we compare the results of our CTMC-QUEST calculations for the three different laser intensities $I = 5, 7.5$, and 10×10^{13} W/cm^2. There is no clear variation in the position of the Cooper minimum between the two highest intensities. However, at the lowest intensity the minimum is shifted to lower energies (52.7 eV). This reflects the intensity dependence of the shape of the rescattering wave packet. Our experiments are consistent with the lack of variation of the minimum between 7.5×10^{13} and 1.0×10^{14} W/cm^2. At lower intensities we observed a slight downshift of the minimum which could be the signature of the modification of the wave packet described by the theoretical results.

V. CONCLUSION

In this paper we have studied the link between photoionization and high-order -harmonic generation by focusing on the Cooper minimum in argon. This structural feature is common to the two processes but, while the position of the minimum is observed between 48 and 49 eV in total photoionization cross sections, we measured it at 53.8 eV with HHG. By performing a systematic experimental study using 1800 nm laser pulses, we have concluded that the position of the Cooper minimum was independent of gas pressure and focusing conditions and, to a large extent, of laser intensity.

The observed shift of the Cooper minimum is partly due to the fact that the recombination process involved in HHG is the inverse process of a particular case of photoionization, in which the quantization axis of the atomic orbital, electron ejection direction, and XUV photon polarization are parallel. We have checked the influence of these parameters by manipulating the electron trajectory using ellipticity, and have observed similar effects in recombination dipole moments and experimental harmonic spectra.

The dipole moment is not sufficient to determine accurately the harmonic spectrum; an additional shift of the Cooper minimum is due to the structure of the recombining electron wave packet.

In order to reproduce the experimental observations, we have developed a model based on the combination of CTMC and quantum electron scattering techniques. CTMC-QUEST takes into account the role of the ionic potential on the 3D trajectories of the electrons in the continuum. The recombination dipole moment corresponding to each individual electron trajectory is quantum mechanically computed taking into account the recollision angle with respect to the quantization axis. This procedure enables us to obtain a very satisfactory agreement between theoretical and experimental spectra. It further allows to unambiguously discriminate between short, long, and multiple return trajectories contributing to the recollision wave packet.

Our results show that accurate high-order-harmonic spectroscopy can be performed using long wavelength lasers. The degree of precision reached by the experiment has allowed us to refine our theoretical modeling. Taking advantage of the versatility and ease of implementation of the CTMC-QUEST approach, we are now working on its extension to elliptically polarized pulses and polyatomic molecules, in the perspective of achieving a complete 3D description of the generation process [14].

ACKNOWLEDGMENTS

We acknowledge financial support from the ANR (ANR-08-JCJC-0029 HarMoDyn) and from the Conseil Regional d'Aquitaine (20091304003 ATTOMOL and COLA project). We also thank Valérie Blanchet, Nirit Dudovich, Dror Shafir, and Andrew Shiner for fruitful discussions.

[1] P. B. Corkum, Phys. Rev. Lett. **71**, 1994 (1993).
[2] K. J. Schafer, B. Yang, L. F. DiMauro, and K. C. Kulander, Phys. Rev. Lett. **70**, 1599 (1993).
[3] C.-G. Wahlstrom, J. Larsson, A. Persson, T. Starczewski, S. Svanberg, P. Salieres, P. Balcou, and A. L'Huillier, Phys. Rev. A **48**, 4709 (1993).
[4] J. W. Cooper, Phys. Rev. **128**, 681 (1962).
[5] M. Lein, N. Hay, R. Velotta, J. P. Marangos, and P. L. Knight, Phys. Rev. A **66**, 023805 (2002).
[6] J. Itatani, J. Levesque, D. Zeidler, H. Niikura, H. Pepin, J. C. Kieffer, P. B. Corkum, and D. M. Villeneuve, Nature (London) **432**, 867 (2004).
[7] T. Kanai, S. Minemoto, and H. Sakai, Nature (London) **435**, 470 (2005).
[8] C. Vozzi *et al.*, Phys. Rev. Lett. **95**, 153902 (2005).
[9] W. Boutu *et al.*, Nat. Phys. **4**, 545 (2008).
[10] O. Smirnova, Y. Mairesse, S. Patchkovskii, N. Dudovich, D. Villeneuve, P. Corkum, and M. Y. Ivanov, Nature (London) **460**, 972 (2009).
[11] H. J. Wörner, J. B. Bertrand, P. Hockett, P. B. Corkum, and D. M. Villeneuve, Phys. Rev. Lett. **104**, 233904 (2010).
[12] R. Torres *et al.*, Phys. Rev. A **81**, 051802 (2010).
[13] M. C. H. Wong, J.-P. Brichta, and V. R. Bhardwaj, Phys. Rev. A **81**, 061402 (2010).
[14] A.-T. Le, R. R. Lucchese, S. Tonzani, T. Morishita, and C. D. Lin, Phys. Rev. A **80**, 013401 (2009).
[15] S. Ramakrishna, P. A. J. Sherratt, A. D. Dutoi, and T. Seideman, Phys. Rev. A **81**, 021802 (2010).
[16] B. K. McFarland, J. P. Farrel, P. H. Bucksbaum, and M. Gühr, Science **322**, 1232 (2008).
[17] S. Haessler *et al.*, Nat. Phys. **6**, 200 (2010).
[18] Y. Mairesse *et al.*, Phys. Rev. Lett. **104**, 213601 (2010).
[19] S. Sukiasyan, S. Patchkovskii, O. Smirnova, T. Brabec, and M. Y. Ivanov, Phys. Rev. A **82**, 043414 (2010).
[20] B. A. Sickmiller and R. R. Jones, Phys. Rev. A **80**, 031802 (2009).
[21] G. V. Marr and J. V. West, At. Data Nucl. Data Tables **18**, 497 (1976).

[22] J. Samson and W. Stolte, J. Electron Spec. Relat. Phen. **123**, 265 (2002).
[23] R. Abrines and I. C. Percival, Proc. Phys. Soc. **88**, 861 (1966).
[24] C. Winterfeldt, C. Spielmann, and G. Gerber, Rev. Mod. Phys. **80**, 117 (2008).
[25] M. Lewenstein, P. Balcou, M. Y. Ivanov, A. LHuillier, and P. B. Corkum, Phys. Rev. A **49**, 2117 (1994).
[26] H. J. Wörner, H. Niikura, J. B. Bertrand, P. B. Corkum, and D. M. Villeneuve, Phys. Rev. Lett. **102**, 103901 (2009).
[27] P. Colosimo *et al.*, Nature Phys. **4**, 386 (2008).
[28] C. Vozzi, F. Calegari, F. Frassetto, L. Poletto, G. Sansone, P. Villoresi, M. Nisoli, S. De Silvestri, and S. Stagira, Phys. Rev. A **79**, 033842 (2009).
[29] A. D. Shiner, C. Trallero-Herrero, N. Kajumba, H.-C. Bandulet, D. Comtois, F. Legare, M. Giguere, J.-C. Kieffer, P. B. Corkum, and D. M. Villeneuve, Phys. Rev. Lett. **103**, 073902 (2009).
[30] CXRO [http://www-cxro.lbl.gov/] "Center for x-ray optics."
[31] P. Salières, A. L'Huillier, and M. Lewenstein, Phys. Rev. Lett. **74**, 3776 (1995).
[32] J. P. Farrell, L. S. Spector, B. K. McFarland, P. H. Bucksbaum, M. Gühr, M. B. Gaarde, and K. J. Schafer, e-print arXiv:1011.1297.
[33] B. H. Bransden and C. J. Joachain, *Physics of Atoms and Molecules* (Peerson Education Limited, 2003).
[34] H. G. Muller, Phys. Rev. A **60**, 1341 (1999).
[35] B. Pons, Phys. Rev. Lett. **84**, 4569 (2000).
[36] B. Pons, Phys. Rev. A **63**, 012704 (2000).
[37] A.-T. Le, T. Morishita, and C. D. Lin, Phys. Rev. A **78**, 023814 (2008).
[38] F. A. Parpia, W. R. Johnson, and V. Radojevic, Phys. Rev. A **29**, 3173 (1984).
[39] L. Young *et al.*, Phys. Rev. Lett. **97**, 083601 (2006).
[40] Z.-H. Loh, M. Khalil, R. E. Correa, R. Santra, C. Buth, and S. R. Leone, Phys. Rev. Lett. **98**, 143601 (2007).
[41] D. Shafir, Y. Mairesse, D. M. Villeneuve, P. B. Corkum, and N. Dudovich, Nat. Phys. **5**, 412 (2009).
[42] P. Antoine, B. Carré, A. L'Huillier, and M. Lewenstein, Phys. Rev. A **55**, 1314 (1997).
[43] Y. Mairesse, N. Dudovich, J. Levesque, M. Ivanov, P. Corkum, and D. Villeneuve, New J. Phys. **10**, 025015 (2008).
[44] J. Levesque, D. Zeidler, J. P. Marangos, P. B. Corkum, and D. M. Villeneuve, Phys. Rev. Lett. **98**, 183903 (2007).
[45] M. V. Frolov, N. L. Manakov, T. S. Sarantseva, and A. F. Starace, J. Phys. B **42**, 035601 (2009).
[46] M. V. Frolov, N. L. Manakov, T. S. Sarantseva, M. Y. Emelin, M. Y. Ryabikin, and A. F. Starace, Phys. Rev. Lett. **102**, 243901 (2009).
[47] T. Morishita, A. T. Le, Z. Chen, and C. D. Lin, Phys. Rev. Lett. **100**, 013903 (2008).
[48] N. Stolterfoht, R. D. Dubois, and R. D. Rivarola, *Electron Emission in Heavy Ion–Atom Collisions* (Springer-Verlag, 1997).
[49] M. B. Shah, C. McGrath, C. Illescas, B. Pons, A. Riera, H. Luna, D. S. F. Crothers, S. F. C. O'Rourke, and H. B. Gilbody, Phys. Rev. A **67**, 010704 (2003).
[50] P. Botheron and B. Pons, Phys. Rev. A **80**, 023402 (2009).
[51] J. S. Cohen, Phys. Rev. A **64**, 043412 (2001).
[52] R. Uzdin and N. Moiseyev, Phys. Rev. A **81**, 063405 (2010).
[53] P. Botheron and B. Pons, Phys. Rev. A **82**, 021404 (2010).
[54] O. Smirnova, M. Spanner, and M. Y. Ivanov, Phys. Rev. A **77**, 033407 (2008).
[55] H. Soifer, P. Botheron, D. Shafir, A. Diner, O. Raz, B. D. Bruner, Y. Mairesse, B. Pons, and N. Dudovich, Phys. Rev. Lett. **105**, 143904 (2010).
[56] D. J. W. Hardie and R. E. Olson, J. Phys. B **16**, 1983 (1983).
[57] M. J. Raković, D. R. Schultz, P. C. Stancil, and R. K. Janev, J. Phys. A **34**, 4753 (2001).